International Journal of Heat and Mass Transfer 52 (2009) 4484–4499

Contents lists available at ScienceDirect

International Journal of Heat and Mass Transfer

journal homepage: www.elsevier.com/locate/ijhmt

Heat transfer of impinging jet-array onto concave- and convex-dimpled surfaces with effusion

Shyy Woei Chang [a,*], Hsin-Feng Liou [b]

[a] Thermal Fluids Laboratory, National Kaohsiung Marine University, No. 142, Haijhuan Road, Nanzih District, Kaohsiung City 81143, Taiwan, ROC
[b] Department of Marine Engineering, National Kaohsiung Marine University, Taiwan, ROC

ARTICLE INFO

Article history:
Received 4 December 2008
Received in revised form 18 March 2009
Accepted 18 March 2009
Available online 8 May 2009

Keywords:
Effusion impacts
Impinging jet-array
Dimpled impinging surface

ABSTRACT

Heat transfer measurements for an impinging jet-array onto two enhanced surfaces using concave and convex dimples with effusion are performed to acquire the detailed Nusselt number (Nu) distributions. The study focuses on the effects of effusion on local and area-averaged heat transfer performances with jet Reynolds number (Re) and separation distance (S/D_j) varying in the ranges of $5000 \leqslant Re \leqslant 15{,}000$ and $0.5 \leqslant S/D_j \leqslant 10$. For each Re and S/D_j tested, three sets of heat transfer data are acquired from each effused impinging surface at three eccentricities (E) between jet-center and dimple-center of 0, 1/4 and 1/2 dimple-pitch (H). Effects of effusions on heat transfer performances are revealed by comparing the Nu measurements obtained from each dimpled surface with and without effusion. A set of selected experimental data illustrates the influences of effusion on the interdependent impacts of surface topology, Re, S/D_j and E/H on the detailed Nu distributions and the area-averaged Nu over the central jet region ($\overline{Nu}_C$). Relative enhancement in heat transfer convected by each dimpled surface with and without effusion from the reference $\overline{Nu}_C$ obtained from the smooth-walled impinging surface without effusion is examined for each Re, S/D_j and E/H tested. To assist the engineering applications, six $\overline{Nu}_C$ correlations for two effused surfaces with concave and convex dimples at $E/H = 0$, 1/4 and 1/2 are individually obtained using Re and S/D_j as the controlling parameters.

1. Introduction

Many industrial applications employ impinging jets to gain high heat/mass transfer performances. Flow structures of the impinging jets are generally characterized into free-jet, stagnation and wall-jet regions. With a single impinging jet of relatively large separation distance, the maximum Nusselt number (Nu) on the impinging surface develops at the stagnation point away from which the local Nu follows the typical bell-shaped decay in the radial direction. With large heat transfer areas, impinging jet-arrays are used but their heat transfer enhancement (HTE) performances are complicated by the jet-to-jet interactions prior to, upon and after the impingement. Prior to impingements, jets from an array are convected in the free-jet region where the heat and mass transfer between the jets and their surrounding flow prevail. These pre-impingement transfer mechanisms affect the temperatures and momentum of free jets by way of jet-distortion, diffusion and entrainment that modify the impingement heat transfers. For laboratory conditions with isothermal flows, the influences of such pre-impingement interactions on *jet-temperatures* are not simulated. Factors putting forth the direct influences on the pre-impingement flow interactions include jet entrainments [1], crossflows [2–6] and degrees of confinements [7–10]. With high degrees of confinements and limited exits for spent flows [2–5,8], the directions of spent flow are unified to formulate crossflows which diffuse or deflect free-jets and affect jet temperatures via the pre-impingement interactions. In this regard, high jet Reynolds numbers (Re) and small separation distances (S) between nozzle and target plates are prone to the generation of strong crossflows. The arrangement of spent flow exit(s) that affects the strength and directions of crossflows can considerably affect Nu distributions over the impinging surface [8]. Flow regions with high jet-to-crossflow interactions generally coincide with the low Nu; and the stagnation Nu peaks decay in the downstream direction of the crossflow [10]. Although local Nu on the impinging surface is generally reduced by the crossflow, but it can be enhanced when S becomes very small ($S/D_j < 1$) [2,3,6,9]. Upon and after impingement, the intricate wall-jet and jet-to-jet interactions are coupled to affect the flow structures and thereby affect the heat transfer performance of an impinging jet-array. Flow interactions upon and after impingements are influenced by nozzle geometry [10–12], jet-array arrangement [13–15], separation distance [9–17], incidence angle of jets [18], free and submerged conditions [19], topology of impinging surface [20–30] and the treatment for spent fluid removal [31,7,32–34]. When Re and S are, respectively, large and

* Corresponding author.
E-mail address: swchang@mail.nkmu.edu.tw (S.W. Chang).

0017-9310/$ - see front matter © 2009 Elsevier Ltd. All rights reserved.
doi:10.1016/j.ijheatmasstransfer.2009.03.050

Nomenclature

A, B	Coefficient and exponent in $\overline{Nu}_C$ correlation
A_C	Area of central jet region on impinging surface (m^2)
D_j	Diameter of jet nozzle for baseline array (m)
D_p	Spherical diameter of concave or convex dimple (m)
E	Eccentricity between jet-center and dimple-center (m)
k_f	Thermal conductivity of fluid (W/mK)
H	Jet-to-jet pitch (m)
$\dot{M}$	Total mass flow rate issued from jet-array
Nu	Local Nusselt number = $qD_j/k_f(T_w - T_j)$
$\overline{Nu}_C$	Area-averaged Nusselt number over central jet region
q	Convective heat flux (W/m^2)
Re	Reynolds number = $(4/12\pi)(\dot{M}/\mu D_j)$
S	Separation distance from nozzle exit to flat portion on dimpled surface (m)
T_j	Fluid temperature at exit of nozzle (K)
T_f	Film temperature = $(T_w + T_j)/2$ (K)
T_w	Wall temperature (K)
X, Y	Dimensionless location (x/D_j, y/D_j)
x, y	Coordinate system with origin at the center of dimpled surface (m)
Greek symbols	
μ	Fluid dynamic viscosity (kg/ms)
ρ	Fluid density (kg/m^3)

small [14], a ring of secondary *Nu* peak is developed that surrounds each confined jet in the interaction zone due to the boundary layer transition triggered by the accelerated and decelerated radial flows [7,12,14]. As such boundary layer transition in the interaction zone of wall-jet region is triggered by the jet-to-jet interactions under the regionally confined conditions due to small S and jet-to-jet spacings (H), these secondary *Nu* peaks decrease with the increases of S and H [14]. Further increase of S can transit the confined wall-jet flow in an array from the submerged condition to the free surface jet-flow. Therefore S and H are two decisive geometric factors for determining the submerged and free-jet conditions which can result in different heat transfer characteristics over the impinging surface [19].

When the crossflow deteriorates heat transfer of an impinging jet-array, the crossflow effect can be minimized by arranging the additional exits for spent flows, such as providing the openings through impinging surface, nozzle plate or carving grooves on nozzle plate [7,31–34]. In general, the effect of spent fluid removal is higher for smaller jet-to-jet spacings due to the more intense jet interactions and crossflow effects [33]. In this regard, the use of grooved nozzle plate could elevate local *Nu* over the most confined central jet region due to the favorable treatment for spent fluid removal that also enriched the central jet momentum via the pre-impingement entrainment at small S [17]. With the spent fluid discharged through the nozzle plate [32], the flow re-entrainment is reduced and the area-averaged *Nu* is elevated as $S/D_j < 2$. But with very small S ($S/D_j \sim 0.25$), the spent fluid removal lowers the local *Nu* in the localities below the spent air holes due to the detachment of wall jets when the spent fluid is directed away from the impinging surface towards the spent air holes [33]. The neutralized HTE performances by allocating venting holes through the nozzle plate at conditions of $S/D_j \geqslant 2$ [32] and the reduced local *Nu* under the venting holes with S/D_j about 0.25 [33] enlightened the undesirable effects of losing mass flows that wash over the impinging surface through the venting holes on the nozzle plate or through the impinging surface. When occasions demand for employing the effusion holes through the impinging surface, such as the effusion cooling networks for the combustion chamber in a gas turbine engine, the effects of effusion on heat transfer of the impinging jet array need to be examined, especially when the topologies of the impinging surface is modified for reinforcing the strength of structure or for enhancing the HTE effects.

Few studies investigated the heat transfer performance of the impinging jet and jet-array with complex topologies over the impinging surface. These modified impinging surfaces resemble electronic component and pin-fin array [22,23], cylindrical [25], rib-roughened [21,24,26] and dimpled [27–30] surfaces. For an axisymmetric impingement jet onto a pedestal [22], the jet-flow decelerates as it impinges on the top face of the pedestal and generates a very thin boundary layer near the sharp corner of the pedestal where the flow separation occurs. Due to such sharp-edge tripped flow separation, a highly turbulent region develops along the separated shear layer and reattaches to the base plate that produces high *Nu* locus near the reattachment point. But the recirculation zones are formulated at both sides of the pedestal and turn into thermal barriers. As a result, the local minimum and maximum *Nu* levels, respectively, developed on the bottom corner of the pedestal and at the location slightly upstream of the reattachment point [25]. With a single into impinging onto the surface roughened by repeated rectangular ribs [21], the wall-jet flow can be trapped in the cavity between the neighboring ribs to prevent the penetration of impinging jet into the cavity and cause local heat transfer impediments within. By modifying the sharp edged topologies of the impinging surfaces into the circular or spherical shapes [25,29], the separated wall-jet flows at the sharp edges of the protrusions [21,22,24,26] are diminished but replaced by the vortical and/or bursting flows over the curved and dimpled surfaces [25,29]. With the single jet impinging onto a convex cylinder, the spent flow underneath the separated shear layer is reversed and formed a wake which boosts local flow velocities and elevates local *Nu* [25]. With the impinging jet-array onto the convex-dimpled surface with different eccentricities between the centers of jets and dimples [29], the moderated jet-to-jet interactions and the shrinkage of the inter-jet region together with the elevated *Nu* over the stagnation regions could improve the HTE performance.

With impinging jet(s) onto concavities, the wakes and/or the bursting phenomena associated with the wall-jet flows over these concavities produce vortices that affect the impingement heat transfer. Recently, the heat transfer researches for impinging jet(s) over the concave-dimpled surface were widely performed for the cooling applications of gas turbine blade and electronic components [27,28,30]. With small S ($S/D_j \leqslant 2$), the dimple-induced bursting phenomena can undermine impingement heat transfer from the flat surface conditions [27,30]. Further increase of S/D_j can lead the area-averaged *Nu* over the confined jet region on the concave-dimpled surface to be improved from the smooth-walled level. With the increased areas by these concave dimples considered, the transferred thermal power over the concaved-dimpled surface are consistently higher than the smooth-walled counterparts [30].

Although various factors examined previously have shown different degrees of impacts on heat transfer, *Re*, Prandtl number (Pr) of coolant, S/D_j and a set of predefined jet-array configurations are generally selected as the controlling parameters to characterize the heat transfer performance of an impinging jet-array [1–34]. It is also worth noting that the concave dimple is an indented surface and the convex surface is a protruded one. But for the convenience

of abbreviations, the concave and convex dimples are referred to the indented and protruded surfaces hereafter. This experimental study performs the detailed *Nu* measurements over the concave- and convex-dimpled impinging surfaces with and without effusion. Influences of effusion on heat transfer performances over the concave- and convex-dimpled impinging surfaces are particularly examined with a set of heat transfer correlations derived to assist the design applications.

2. Experimental details

2.1. Experimental facilities

Fig. 1 depicts (a) the jets impingement test rig and (b) the configurations of the jet-array with the dimpled impingement heating surface on which the *X*–*Y* coordinate system is indicated. As shown in Fig. 1a, the dry and cooled airflow is guided through a set of mass flow meter and needle valve where the airflow rate is, respectively, metered and adjusted and then channeled through a 200 mm long, 15 mm wide square sectioned flow calming tube (1) into the flow settling chamber (2). The orifice plate (3) with the thickness of two jet diameters is fitted at the wide end of the divergent flow chamber (2) and constituted by twelve equally spaced in-line orifices of 3 mm in diameter (D_j) which is the characteristic length for defining *Re* and *Nu*. Jet-to-jet spacing (H/D_j) for this 3×4 jet array is 4. The *X*- and *Y*-wise pitches between two jet-centers and two dimple-centers are both 4 D_j. The diameter of each dimple (D_p) is 12 mm. Effusion holes of 1.5 mm in diameter are drilled through the impinging foil at the geometric centers of four surrounding dimples. As shown in Fig. 1b, the jets issued from the orifice plate impinge onto the very thin (0.1 mm) and 65 mm wide stainless-steel dimpled heating foil (7). The central confined jet region is indicated in Fig. 1b. The area-averaged *Nu* over this central confined jet region is defined as $\overline{Nu}_C$. The 4×3 array of equal-spaced surface dimples with the maximum depth (height) of 1/4 D_p are forged from a continuous thin stainless steel foil. As the var-

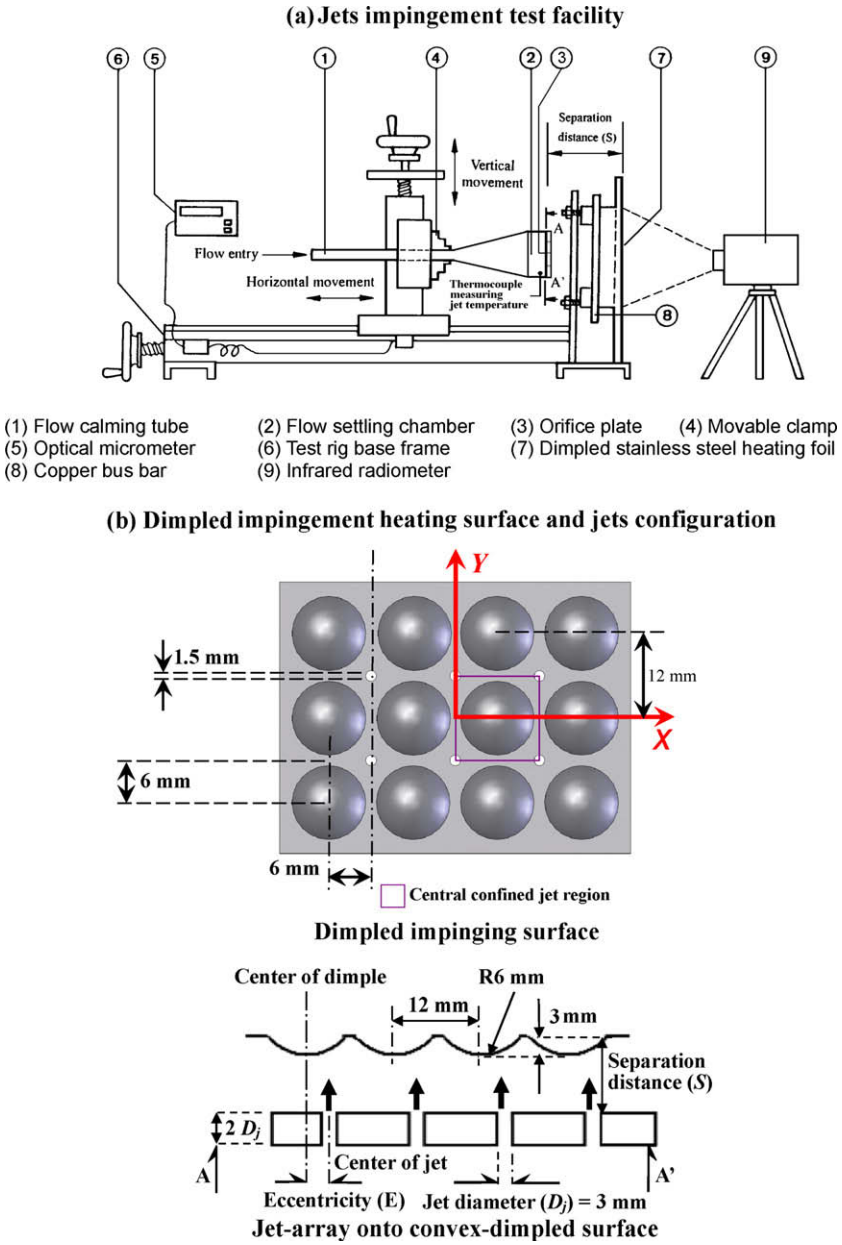

Fig. 1. (a) Jets impingement test facility (b) geometries of dimpled impinging surface with effusion holes.

iation of the thickness over the entire dimpled foil is less than 1%, the maximum non-uniformity in heater power generation due to the different cross-sectional areas between the dimpled and flat sections is about 9.2%. This dimpled stainless steel foil is stretched tightly between two copper bus bars (8) on the test rig, through which the adjustable and metered DC electrical power is applied to generate the Joule heating. For the concave- or convex-dimpled surface with effusion, the heat transfer tests with eccentricities (E) of 1/4 and 1/2 H are performed by shifting the heating foil horizontally. The foil deflection at the maximum Re and the smallest S is less than 0.025 mm. The detailed temperature distributions over the dimpled impinging surface are imaged by a two-dimensional infrared radiometer (9) that can complete the 239×255 matrix scan in 0.3 s. To minimize the effect of background reflection and increase the emission, the back surface of the dimpled heating foil is painted black.

2.2. Experimental program

This experimental study examines the effect of effusion on heat transfer performances for the impinging jet-array onto the concave- and the convex-dimpled surfaces by comparing the detailed Nu measurements over these dimpled impinging surfaces with and without effusion at $Re = 5000$, 7500, 10,000, 12,500, 15,000 and $S/D_j = 0.5$, 1, 3, 5, 7, 10. At each set of Re and S/D_j examined, three sets of Nu measurements for each dimpled surface at $E/H = 0$, 1/4, 1/2 are obtained. The impacts of Re, S/D_j and E/H on $\overline{Nu}_C$ over the concave- and convex-dimpled surfaces with effusion are parametrically examined after which a set of $\overline{Nu}_C$ correlations are derived. All the Nu distributions are obtained from the steady-state measurements. Steady state is assumed when several successive scan of wall temperatures over the impinging surface are less than 0.3 K for each predefined test condition and generally takes about 30 min to reach after the heating power or the airflow rate is adjusted.

The adiabatic wall temperatures over the impinging surface are measured using the present data acquisition system by way of issuing the jets with no heating power. Over the entire tested conditions, the maximum differences between the adiabatic wall temperature and the jet temperatures are less than 0.2 K so that the reference fluid temperature for defining Nu is selected as the jet temperature (T_j) which is measured by a thermocouple penetrated into the plenum chamber as indicated in Fig. 1a. The temperature dependent fluid properties are evaluated from the local film temperature (T_f) defined as $(T_w + T_j)/2$. The heating area used to define heat flux includes the dimple surfaces. This additional dimpled area includes fin effects to increase the heat-transfer power convected through the flow system. With the fixed heater power of 450 W, the wall-to-jet temperature differences fall in the range of 35.7–61.2 °C. The local Nu over the impinging surface is evaluated as $Nu = qD_j/\{k_f[T_w(X, Y) - T_j]\}$. The convective heat flux (q) is calculated from the total heat flux with the heat-loss flux to be subtracted. The characteristics of external heat-loss flux is determined through a series of calibration tests and the details have been previously reported [29,30]. As T_w distributions over the impinging surface are not uniform, the distribution of local heat-loss flux is accordingly non-uniform, which has led to the maximum non-uniformity of about 5.2% in the convective heat flux (q) over the impinging surface.

For an impinging jet-array, the pressure distribution over the impinging surface varies with the flow and geometric conditions such as Re, S/D_j, E/H, topology of the impinging surface and the effusions. As a result, the mass flow rate through each nozzle in the orifice plate is different and is functionally controlled by Re, S/D_j, E/H, topology of the impinging surface [8] and effusion. By fixing the flow and associated geometrical parameters, the flow field over the impinging surface is accordingly generated and the influences of varying Re, S/D_j, E/H on heat transfer performances over the dimpled surfaces with effusion are examined. Re is conveniently specified as $(4/12\pi)(\dot{M}/\mu D_j)$ where $\dot{M}$ is the total mass-flow-rate fed to the twelve jets. The discharge coefficients of the orifice nozzle for all test conditions are estimated by normalizing the measured coolant mass flow rate through each orifice defined as $\dot{M}/12$ to the theoretical value determined from the measured pressure ratio across the orifice plate, which fall in the range of 0.8–0.85 for the present test rig. The experimental repeatability of the temperature measurement using the present infrared radiometer has been previously reported [12] with the maximum uncertainty in T_w measurement of ±0.7 °C. This uncertainty in T_w measurement is the major source to attribute the uncertainties for Nu and the fluid properties determined from the local film temperature. Following the policy of ASME J. Heat Transfer on reporting the uncertainties in experimental measurements and results [35], the maximum uncertainty associated with Nu and Re were estimated as ±9.3% and ±7.2%, respectively.

3. Results and discussion

3.1. General heat transfer performance over impinging dimpled surfaces with effusion

The present heat transfer results generated from the dimpled impinging surfaces with effusion are comparatively examined with our previous measurements [29,30] obtained from the same dimpled surfaces without effusion. The general heat transfer characteristics of the impinging jet-array onto the dimpled surfaces with effusion are comparatively illustrated using three sets of Nu distributions collected at $S/D_j = 3$ and $Re = 12{,}500$ with $E/H = 0$, 1/4 and 1/2, as depicted in Fig. 2. As seen in Fig. 2, the jets, effusion-holes and dimples are symmetrical about Y axis. Therefore the Nu distributions are symmetrical about Y. The comparisons of Nu distributions obtained from the dimpled surfaces with and without effusion are made by comparing one half of each Nu scan. In each plot compared in Fig. 2, the area-averaged Nu over the central confined jet region ($\overline{Nu}_C$) with and without effusion are indicated. Generally, a heat transfer hump centered on each stagnation point along with the concave Nu profiles at the inter-jet regions between four surrounding stagnation points are observed in Fig. 2. Even with the concave or convex dimples, such heat transfer characteristics inherited from the impinging jet array still remain persistent. By using the concave or convex dimples or adjusting E/H, the different surface topologies encountered by the wall-jet flows upon and after impingements have led to various degrees of heat transfer modifications in the stagnation and the inter-jet regions, respectively. With no effusion, the recirculating flows are likely to develop inside the concave dimples so that the $\overline{Nu}_C$ over the impinging surfaces with concave dimples are generally lower than their counterparts with convex dimples. Ekkad and Kontrovitz [27] have attributed the lower heat transfer rates over the concave-dimpled impinging surface to the bursting phenomena that produce the disturbances on the impingement jet structures. With effusion, the regional heat transfer impediments over the inter-jet regions caused by the jet-to-jet interferences after impingement are extended from all the non-effusion results. Such heat transfer phenomenon over the impinging surface is triggered by effusion through the dimpled surfaces as the major drawback for HTE performances. As compared in Fig. 2 with $S/D_j = 3$ and $Re = 12{,}500$, the effusion-driven heat transfer impediments perform differently between the impinging surfaces with concave and convex dimples and are E/H dependent. The worst heat transfer scenarios with effusion through the concave- or convex-dim-

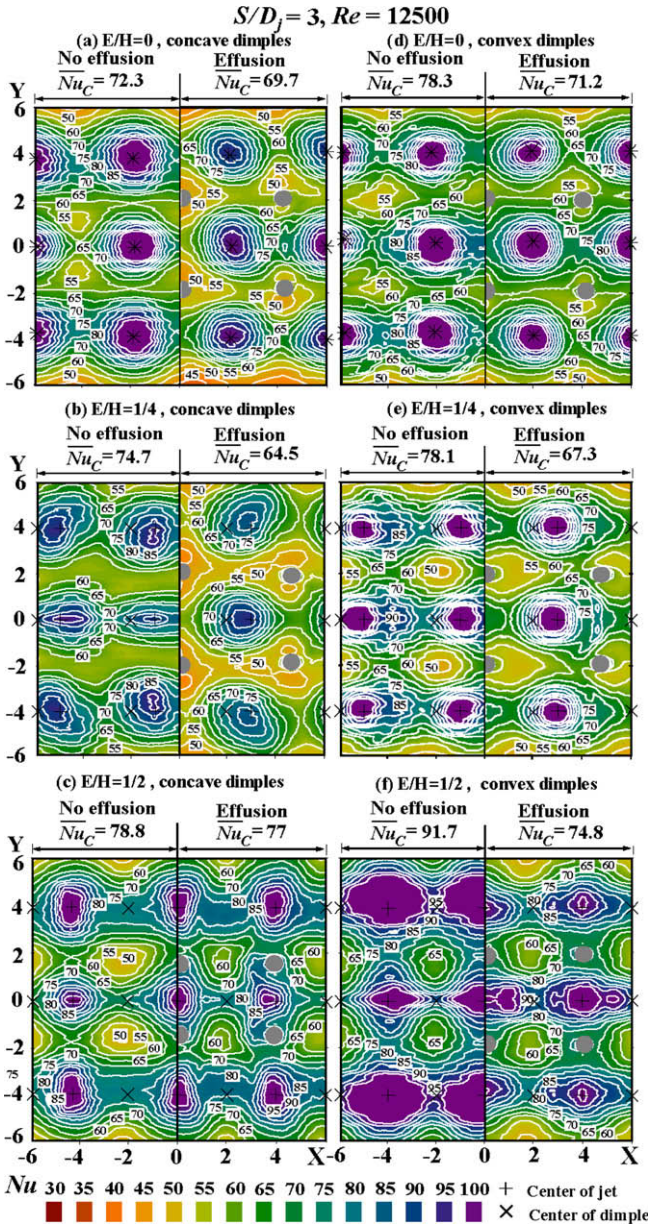

Fig. 2. Detailed *Nu* distributions over concave- and convex-dimpled surfaces with and without effusion at S/D_j = 3, *Re* = 12,500.

pled surfaces resolve at E/H = 1/4 as seen in Fig. 2b and e. With E/H = 1/2, the *Nu* levels over the inter-jet regions on the concave-dimpled surface with effusion, as compared in Fig. 2c, are elevated from the non-effusion counterparts; but the high *Nu* regions around the stagnation points on the concave-dimpled surface with effusion are slightly shriveled from the non-effusion scenarios. Over the convex-dimpled surface with E/H = 1/2 as compared in Fig. 2f, the effusion-driven heat transfer impediments over the inter-jet regions become less effective. But, as compared in Fig. 2f with E/H = 1/2, the regions showing the heat transfer humps around the stagnation points are considerably shrunk over the effused surface with convex dimples so that $\overline{Nu}_C$ is considerably reduced from the non-effusion level. Clearly, the impacts of effusion through these dimpled surfaces generally impede the HTE performances of the impinging jet-array due to either the extension of the inter-jet regions or the shrinkage of heat transfer hump around each stagnation point. The heat transfer physic and the degree of impact for such effusion-driven heat transfer impediment is inter-dependent with E/H and surface topology of the impinging surface as demonstrated in Fig. 2, which also vary with *Re* and S/D_j as demonstrated in the later sections.

With considerable confinement for an impinging jet-array either by reducing S/D_j to the order about 0.1 or by limiting/constraining the exits of spent flows [7,32,33], the additional drainage for spent fluid removal is employed with the attempt to improve the regional heat transfer performances over the inter-jet regions by minimizing the jet-to-jet interferences. Nevertheless, with the dimpled impinging surfaces, our later results will show the local *Nu* elevations around each effusion hole due to the mechanisms reported previously [7,32,33]; but the overall *Nu* reductions due to the loss of coolant's mass flux through effusion, as demonstrated in Fig. 2, are revealed here as a result of reductions in the coolant mass flux available in the impinging flow system. Clearly, with the reduced airflow rate due to effusion, the temperatures of jets and wall-jet flows increase accordingly. This in turn elevates T_w over the impinging surfaces with effusion. Such T_w elevation incurs the overall *Nu* reduction over the entire impinging surface with effusion. Particularly, as exemplified in Fig. 2f, the weakened mass fluxes in wall-jet flows due to effusion through the impinging surface have also weakened the momentum required to surge flows onwards the convex dimples with E/H = 1/2 and caused the considerable shrinkage of *Nu* hump around each stagnation point. Justified by the various degrees of moderation in *Nu* hump around each stagnation point as depicted in Fig. 2, the impact of effusion on weakening the momentums of wall-jet flows vary with E/H and the topology of the impinging surfaces. Although these effusion-induced heat transfer impediments due to the loss of coolant mass flux are interdependent with *Re*, S/D_j, E/H and surface topology, the attendant T_w increments, the expansions of inter-jet regions with low *Nu* and the shrinkage of *Nu* hump around each stagnation point as revealed in Fig. 2 require design precautions. The competitive differences between the mechanisms those impede heat transfer performances and improve the transportation of spent flows [7,32,33] play the decisive role on determining the improving or impeding heat transfer impacts by effusion. In what follows, the impacts of S/D_j and *Re* on the heat transfer modifications caused by effusion for the concave- and convex-dimpled impinging surfaces are systematically examined.

3.2. Impacts of S/D_j, *Re* on *Nu* distributions over dimpled surfaces with effusions

The impacts of S/D_j on the effusion-driven heat transfer modifications over the impinging surfaces with the concave and convex dimples are, respectively, examined in Figs. 3 and 4 by comparing the *Nu* distributions over the dimpled surfaces with and without effusion. As described previously, two effusion-driven heat transfer mechanisms, namely the expansion of inter-jet region and the moderation of *Nu* hump around each stagnation point, are triggered by the weakened wall-jet momentums. The impacts of S/D_j on these two heat transfer mechanisms have caused the effusion-driven *Nu* modifications to be dependent on S/D_j as depicted in Figs. 3 and 4 where the *Nu* scans collected at S/D_j = 0.5, 3, 7 are compared. For each comparative group collected with the same E/H at *Re* = 7500, the S/D_j-driven *Nu* modifications are readily seen by viewing the *Nu* plots in the sequent orders of Fig. 3a→d→g (E/H = 0), b→e→h (E/H = 1/4) and c→f→i (E/H = 1/2). Among the three comparative groups with different E/H, the effusion has caused the most (least) impairing impacts on the *Nu* distributions over the concave-dimpled surface with E/H = 1/4 (1/2). As revealed in Fig. 3 for E/H = 0 and 1/4, the expansion of inter-jet region along with the moderations of *Nu* humps around stagnation points remain evident; while only slight moderations in *Nu* humps around stagnation points are observed over the concave-dimpled surface

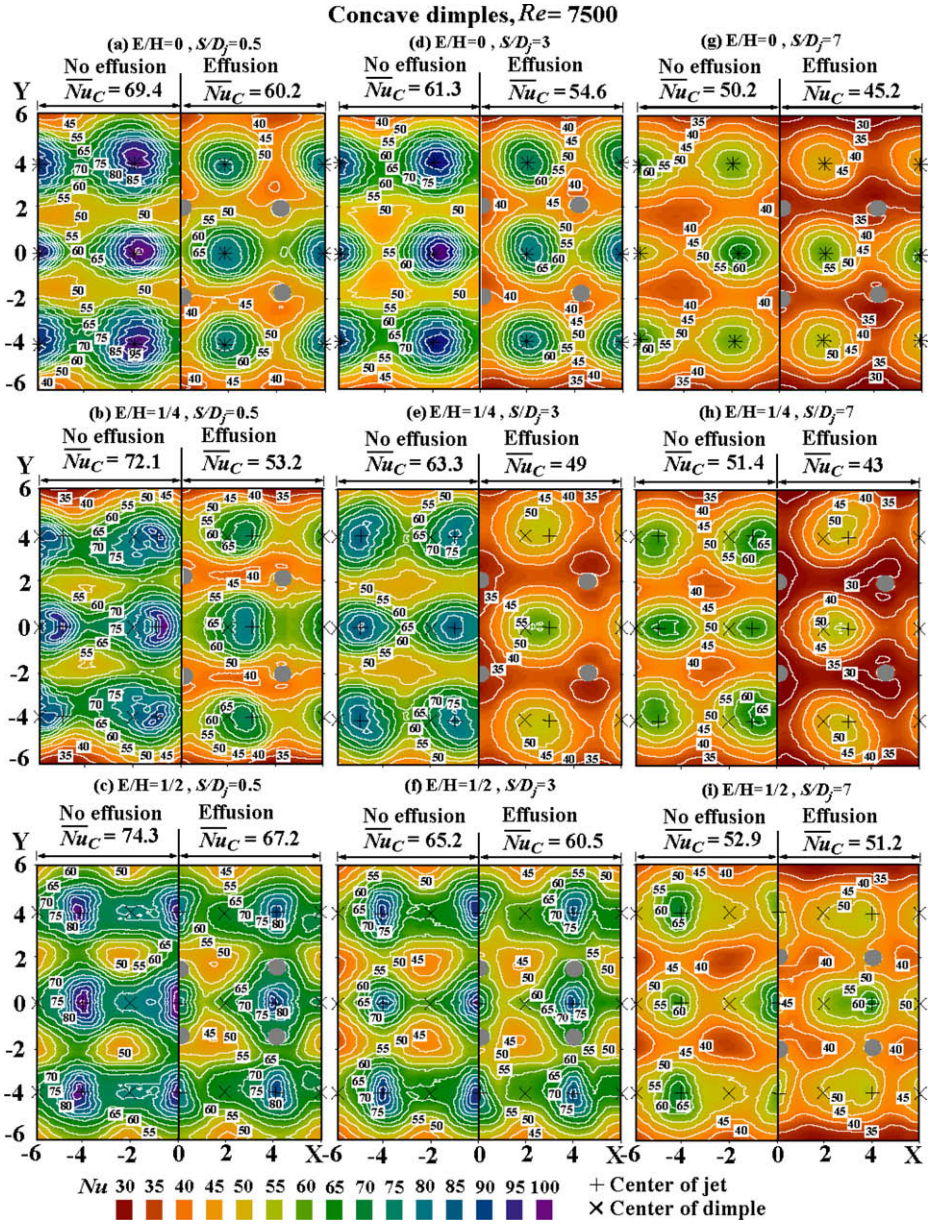

Fig. 3. Detailed *Nu* distributions over concave-dimpled surfaces with and without effusion at $Re = 7500$ for $S/D_j = 0.5$, 3 and 7.

with $E/H = 1/2$. All the $\overline{Nu}_C$ collected from the non-effusion surface as indicated in Fig. 3 are consistently higher than their counterparts obtained from the concave-dimpled surface with effusion. For the present test conditions with concave dimples, the degrees of confinements for the present impinging jet-array are not so severe to grant the beneficial effects by effusion to override the impairing impacts due to the losses of airflow via effusion. In light of the $\overline{Nu}_C$ differences between the effusion and the non-effusion results, using Fig. 3 as in illustrative example, the increase of S/D_j at each selected E/H has systematically reduced the comparative $\overline{Nu}_C$ differences between the results obtained with and without effusion. At $S/D_j = 0.5$, 3, 7 as indicated in each plot of Fig. 3, the differences in $\overline{Nu}_C$ between the impinging surfaces with and without effusion are varied from 13.2% → 11% → 10% ($E/H = 0$), 26% → 22.5% → 16% ($E/H = 1/4$) and 9% → 7% → 3% ($E/H = 1/2$). Such S/D_j-driven pattern has followed by all *Re* tested. The increase of S/D_j from 0.7 to 7 has moderated the effusion-driven heat transfer impacts over the concave-dimpled surface. Local pressure gradients which motivate the effusion flows tend to be weakened by way of increasing S/D_j at a fixed *Re* so that the effusion-driven impacts on $\overline{Nu}_C$ are alleviated.

Over the convex-dimpled surface as shown in Fig. 4, the S/D_j effects on the effusion-driven heat transfer impacts follow the general pattern revealed in Fig. 3 but the interdependency of S/D_j effects on E/H is different from those developed on the concave-dimpled surface. This is demonstrated by examining the differences in $\overline{Nu}_C$ between the convex-dimpled surfaces with and without effusion at $S/D_j = 0.5$, 3, 7. As shown in Fig. 4, the increase of S/D_j from 0.5 → 3 → 7 reduces the percentages of differences in $\overline{Nu}_C$ between the effusion and the non-effusion results following the manner of 11.8% → 10.8% → 9% ($E/H = 0$), 21.5% → 20% → 17% ($E/H = 1/4$) and 25% → 23% → 19% ($E/H = 1/2$). However, although the increase of S/D_j has reduced the $\overline{Nu}_C$ differences between the effusion and non-effusion results, the HTE impacts generated by the impinging jet-array also fade out as S/D_j increases. In Fig. 4, the most (least) impairing impacts on heat transfer perfor-

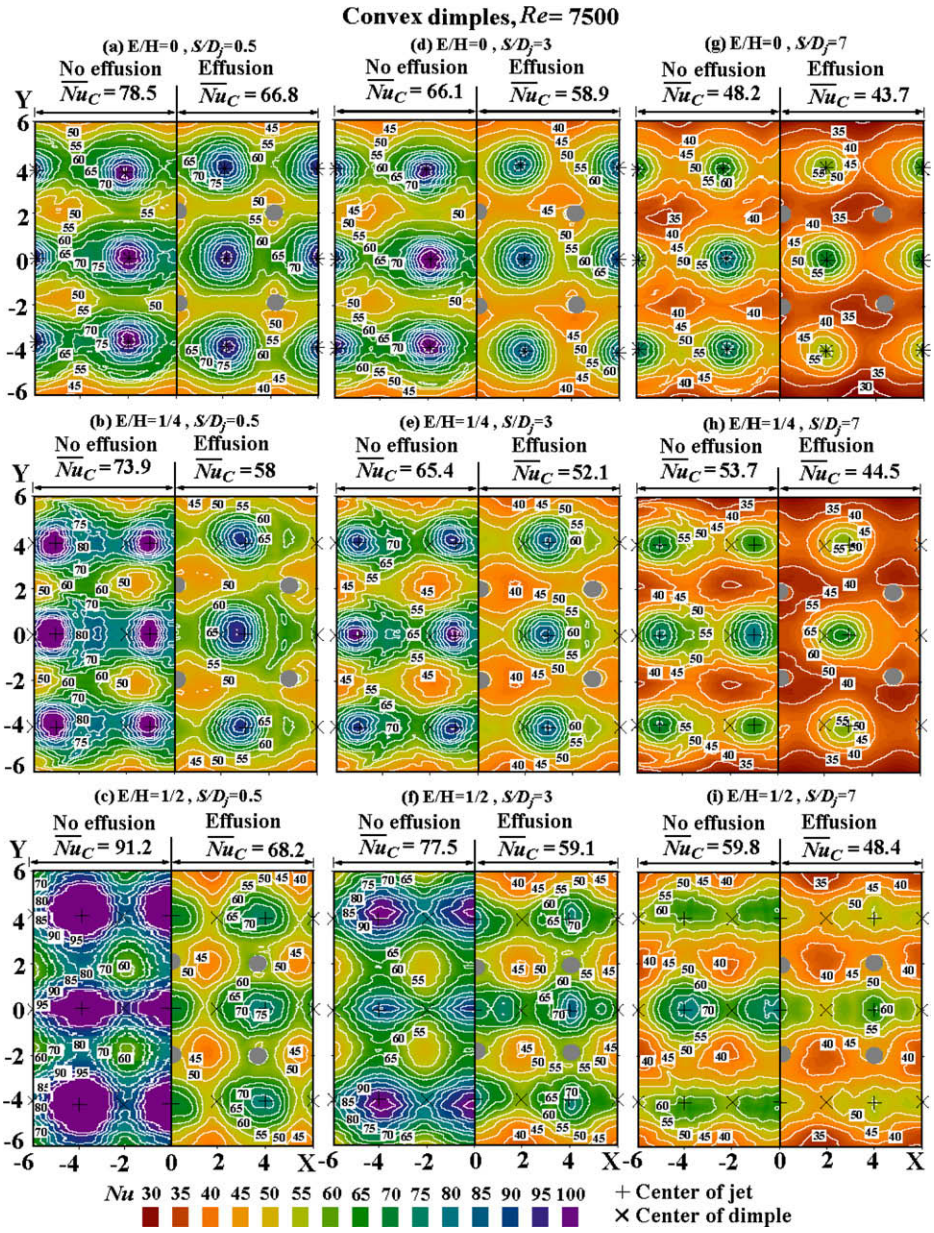

Fig. 4. Detailed *Nu* distributions over convex-dimpled surfaces with and without effusion at $Re = 7500$ for $S/D_j = 0.5$, 3 and 7.

mances over the convex-dimpled surface due to effusion evolve at $E/H = 1/2$ (0). Unlike the heat transfer scenarios compared for the concave-dimpled surface with $E/H = 1/2$ as seen in Fig. 3c→f→i, the effusion-driven expansions of inter-jet regions over the impinging surface with convex dimples still remain evident in contrast with those without effusion as compared in Fig. 4c→f→i ($E/H = 1/2$). When the jets impinge onto the flat portion of the convex-dimpled surface without effusion at $E/H = 1/2$, the up-surging wall-jet flows are directed onward each convex dimple under the downward jet-streams that induces the separated shear layers along which the turbulence intensities and *Nu* are augmented. As a result, for the convex-dimpled surface without effusion, the *Nu* levels over the inter-jet regions at $E/H = 1/2$ are considerably elevated from the counterparts with $E/H = 0$ and 1/4 [29]. But when the wall-jet flows are lack of momentum to upsurge these convex dimples in each inter-jet region due to effusion, these convex dimples turn into obstacles for the convection of spent flows and consequently impair the inter-jet heat transfer performances as depicted in Fig. 4c, 4-f, 4-i. Therefore, the further increase of *Re* from 7500 is likely to assist the wall-jet flows to regain the up-surging momentum over these convex dimples, which consequently alleviates the heat transfer impediments over the inter-jet regions on the convex-dimpled surface with effusion. Such *Re* impacts on the effusion-driven heat transfer modifications are examined by comparing the *Nu* scans obtained from the concave- and convex-dimpled surfaces with and without effusion at *Re* of 5000, 10,000 and 15,000 in Figs. 5 and 6, respectively.

As compared in Figs. 5 and 6 at $S/D_j = 5$ for each E/H examined, the most considerable effusion-driven *Nu* reductions consistently emerge at $Re = 5000$ over the concave- and convex-dimpled surfaces. A systematic increase of *Re* not only consistently reduces the $\overline{Nu}_C$ differences between the effusion and non-effusion results, but also elevates the HTE impacts generated by the impinging jet array for each dimpled surface with and without effusion. Having the wall-jet flows regained the momentums to sweep over each dimpled surface by way of increasing *Re*, the indicative HTE char-

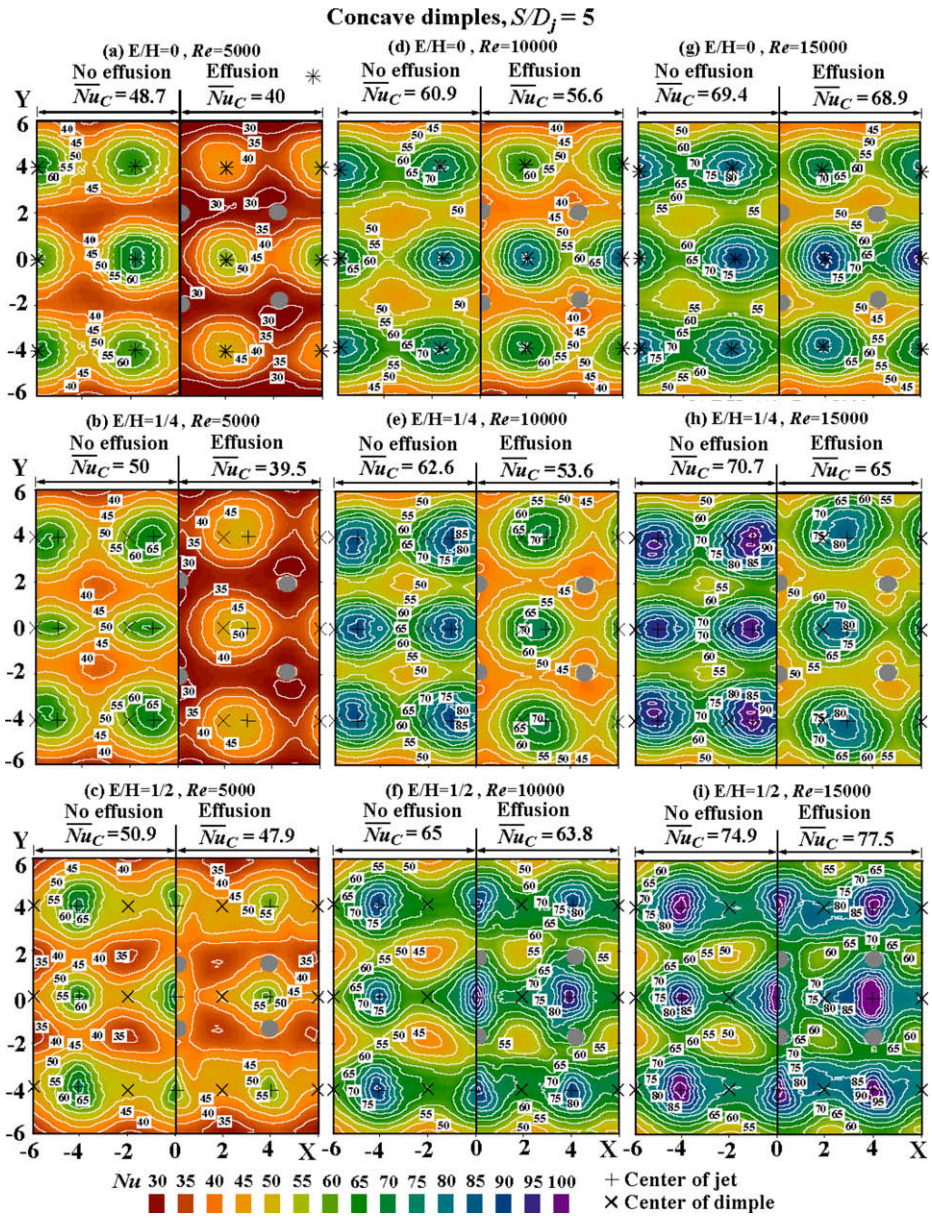

Fig. 5. Detailed *Nu* distributions over concave-dimpled surfaces with and without effusion at $S/D_j = 5$, $Re = 5000$, 10,000 and 15,000.

acteristics for the impinging jet-array onto the dimpled surfaces without effusion [29,30] re-emerge from the effused surface with dimples. In this respect, the expansion of heat transfer hump around each stagnation point along with the shrunk inert-jet region over the dimpled surfaces without effusion at $E/H = 1/2$ have previously reported to elevate *Nu* over the dimpled surfaces from the smooth-walled references [29,30]. As shown in Figs. 5 and 6, the systematic increase of *Re* has led local *Nu* to resolving the more effective HTE impacts around stagnation points and the shriveled inter-jet regions with less *Nu* impediments. As *Re* keeps increasing, the beneficial effusion effects on heat transfer performances [31,7,32] are getting stronger with the tendency to override the impeding *Nu* effects by effusion. Fig. 5i serves as an example to reveal the detailed *Nu* distributions over the concave-dimpled surface when the $\overline{Nu}_C$ on the effused surface rises above the non-effusion level. Clearly, as seen in Fig. 5i, the heat transfer humps around the stagnation points over the concave-dimpled surface with effusion have regained their effectiveness while the *Nu* values over its inter-jet regions are elevated from the non-effusion counterparts. Following such trend of *Re*-driven modifications in *Nu* distributions over each effused surface, the $\overline{Nu}_C$ over the effused surface with dimples tend to rise above the non-effusion references as if *Re* exceeds the critical values for the wall-jet flows to gain sufficient momentums in order to restore the HTE mechanisms tripped by these surface dimples. The varying manners for the percentages of difference in $\overline{Nu}_C$ between the effusion and the non-effusion results against *Re*, as displayed in Fig. 7 using the data collected in Figs. 5 and 6 as an illustrative example, indicates such *Re*-driven effects on $\overline{Nu}_C$ differences between the effusion and non-effusion results. As shown in Fig. 7 for each dimpled surface at all tested *E*/*H*, the differences in $\overline{Nu}_C$ between non-effusion and effusion results consistently decrease as *Re* increases. At each selected *E*/*H*, the $\overline{Nu}_C$ over the concave-dimpled surface recover at the faster rates than their convex counterparts as the higher momentums in wall-jet flows are required to stimulate the HTE impacts triggered by the protruding convex dimples. With $S/D_j = 5$ for the concave-dimpled surface at $E/H = 1/2$ as seen in Fig. 7, the $\overline{Nu}_C$ difference between the effusion and non-effusion

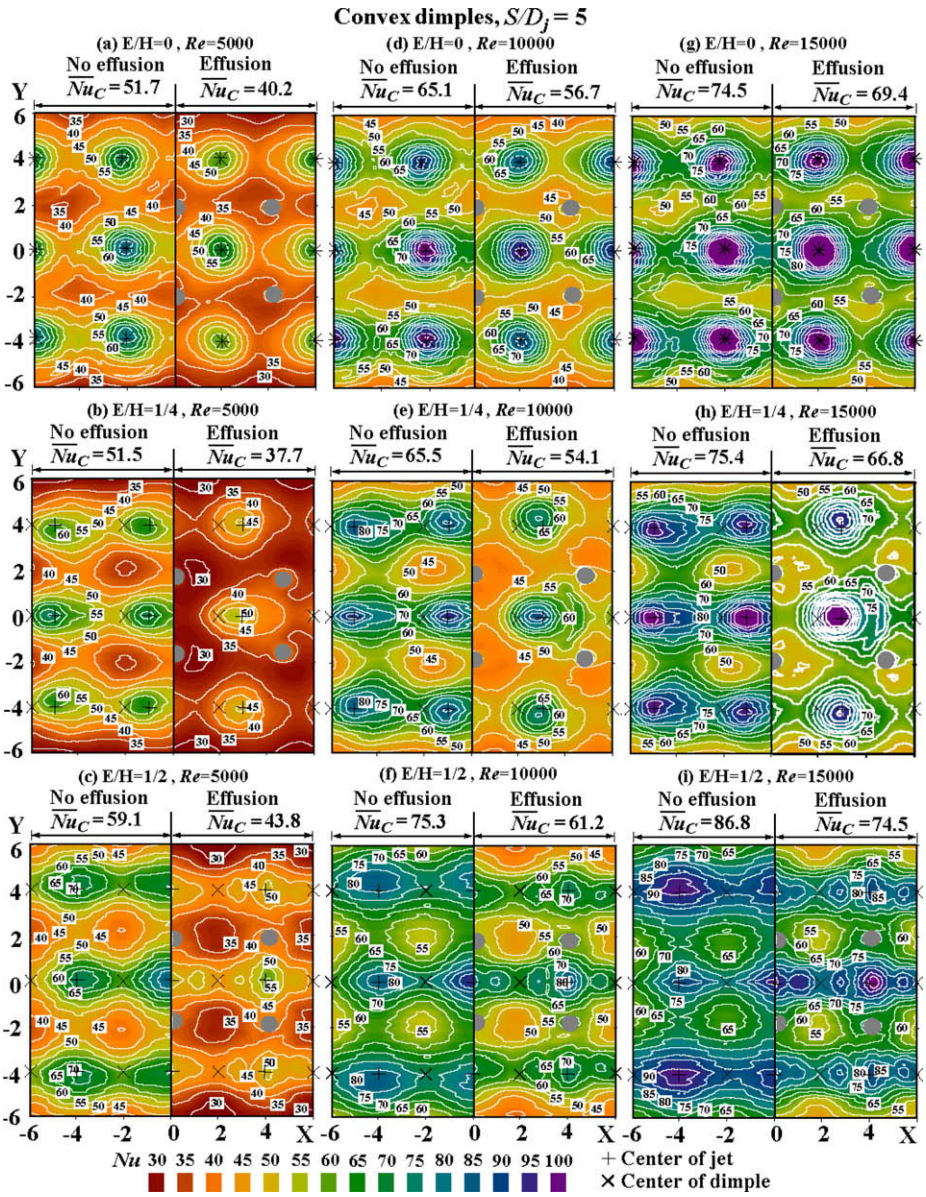

Fig. 6. Detailed *Nu* distributions over convex-dimpled surfaces with and without effusion at $S/D_j = 5$, $Re = 5000$, 10,000 and 15,000.

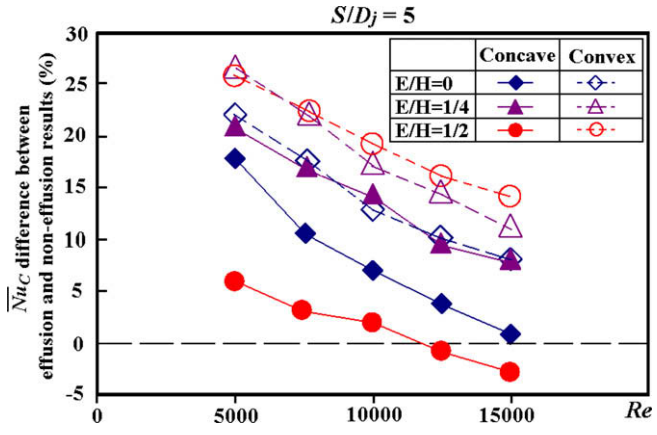

Fig. 7. $\overline{Nu}_C$ differences between effusion and non-effusion results versus *Re* over impinging surfaces with concave and convex dimples at $S/D_j = 5$.

results turns into negative at $Re = 15{,}000$; indicating the higher $\overline{Nu}_C$ over the effused surface at this particular set of test conditions. But the heat transfer tests performed at $E/H = 1/2$ with the convex dimples feature the fully up-surging conditions for the wall-jet flows so that the higher wall-jet momentums are required to stimulate the HTE impacts tripped by these convex dimples. As a result, Fig. 7 depicts the most sluggish *Re*-driven $\overline{Nu}_C$ recovery for the test conditions with convex dimples at $E/H = 1/2$. These aforementioned *Re*-driven data trends summarized in Fig. 7 are followed by all the S/D_j examined. In light of the data trends typified in Fig. 7, the critical *Re* above which the $\overline{Nu}_C$ over an effused dimpled surface turns above the non-effusion level varies with E/H, S/D_j and the topology of the impinging surface.

A more detailed examination of the effusion impacts on heat transfer distributions is conducted by comparing the *Nu* profiles along $X = 0$ and $Y = 0$ axes between the non-effusion and effusion results with concave (Fig. 8a and b) and convex (Fig. 8c and d) dimples. The *Y*-wise *Nu* profiles along $X = 0$ axis at $E/H = 0$, 1/4, 1/2 as

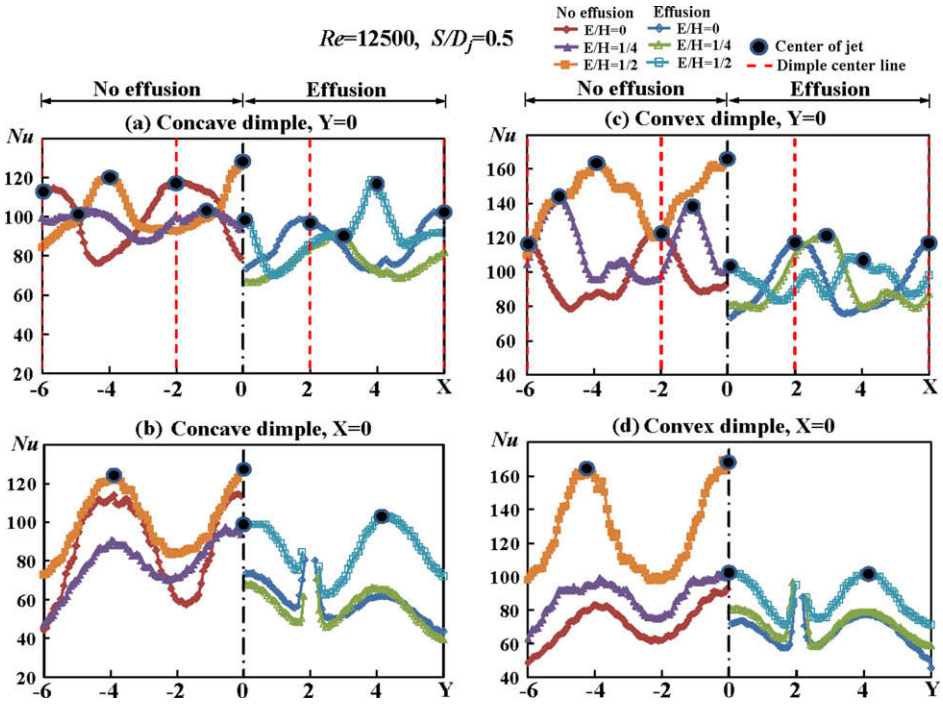

Fig. 8. *X*- and *Y*-wise *Nu* profiles over concave- and convex-dimpled surfaces with and without effusion at $Re = 12{,}500$, $S/D_j = 0.5$.

seen in Fig. 8b and d always traverse the effusion holes to enable the examination of the effusion effects on local *Nu* variations; but are not indicative of the *Nu* profiles along the vertical axes that traverse the stagnation points with $E/H = 0$ and 1/4. Only the *Y*-wise *Nu* profiles collected from $E/H = 1/2$ along $X = 0$ axis can reveal the *Nu* distributions at the stagnation points so that there are only two jet-centers indicated on the *Y*-wise *Nu* profiles in Fig. 8b and d at $E/H = 1/2$. At $Re = 12{,}500$ and $S/D_j = 0.5$, all the plots collected in Fig. 8 consistently show the overall *Nu* reductions in both *X*-wise and *Y*-wise *Nu* profiles over each effused surface from the non-effusion counterparts at the same *E*/*H*. As, respectively, compared in Fig. 8a and c for the *X*-wise *Nu* profiles along $Y = 0$ axis over the concave- and convex-dimpled surfaces, the characteristic patterns of *X*-wise *Nu* variations over the non-effused surface are basically followed by those obtained from the effused surface. But the *X*-wise *Nu* elevations in the inter-jet region between two jet-centers along $Y = 0$ axis over the effused surface with $E/H = 1/2$ in Fig. 8c are more remarkable than its non-effusion counterparts. The similarities in the characteristic *X*-wise *Nu* profiles along $Y = 0$ axis between effusion and non-effusion results for each comparative pair with the same *E*/*H* in Fig. 8a and c reflect the similar heat transfer impacts produced by the identical topologies of the impinging surfaces; while the overall reductions in *Nu* over the effused surface are mainly attributed to the elevated fluid temperatures due to the reductions in airflow rate as a result of effusion. Although the lost airflow from the impingement system via effusion elevates fluid temperatures from the non-effusion conditions for any pre-defined heating power, the local *Nu* elevations surrounding each effusion hole as demonstrated in Fig. 8b and d are evident. The drastic *Nu* elevations around each effusion hole, as consistently seen in Fig. 8b and d, are produced by the effusion-driven local flow accelerations toward each effusion hole, which improves the transportation of spent flow and breaks the boundary layers surrounding each effusion hole. Nevertheless, even if the *Nu* elevations around each effusion hole are considerable, the effective regions for such effusion-driven local HTE impacts over these dimpled surfaces are rather confined to be within one jet diameter. As the overall *Nu* reductions in the *X*-wise and *Y*-wise *Nu* profiles seen in Fig. 8 are not counteracted by the effusion-induced *Nu* elevations over the inter-jet regions, the $\overline{Nu}_C$ over the effused surfaces for all the test conditions specified in Fig. 8 are lower than the non-effusion references.

In order to compare the effusion impacts on *Y*-wise *Nu* profiles corresponding to the jet centers for all three *E*/*H* examined, the alternative *Y* coordinates (y') are specified along the vertical axis on the nozzle-plate that connects three vertically in-lined jets. On each dimpled surface, the *X* locations along the y' axis with $E/H = 0$, 1/4 and 1/2 are, respectively, at $X = 1/2H$, $1/4H$ and 0. This manner of comparison can fairly resolve the *E*/*H* impacts on the *Y*-wise *Nu* variations over the stagnation regions on the dimpled surfaces with and without effusion. The comparisons of *Nu* profiles along the *X* axis at $Y = 0$ and the y' axes between non-effusion and effusion results at $Re = 15{,}000$ with $S/D_j = 0.5$, 1, 5 for three tested *E*/*H* are, respectively, collected in Figs. 9 and 10 for the concave- and convex-dimpled surfaces. In view of the differences in *Nu* profiles along *X* and y' axes between three tested *E*/*H* without effusion as compared in Fig. 9, the most considerable inter-jet heat transfer impediments relative to its stagnation *Nu* levels emerge at $E/H = 0$; while the better heat transfer performances develop at $E/H = 1/2$. On the effused surface with concave dimples, the overall *Nu* are reduced from the non-effusion references along *X* and y' axes for $E/H = 0$ and 1/4 as compared in Fig. 9. With $0.5 \leqslant S/D_j \leqslant 5$ for three *E*/*H* tested, the most and least suppressed heat transfer performances, respectively, resolve at $E/H = 1/4$ and 1/2 on the effused surface with concave dimples. In Fig. 9a–c with $E/H = 1/2$, the *Nu* peak in each *X*-wise *Nu* profile at the jet center along the outer ring of the jet-array on the effused surface at $X = 4$ undergoes the considerable amplification. Along y' axis over the effused surface as shown in Fig. 9d–f, the heat transfer performances at the jet centers as well as over the inter-jet region with $E/H = 1/2$ still remain superior to those with $E/H = 0$ and 1/4. In particular, with $E/H = 1/2$ at $Re = 15{,}000$ and $S/D_j = 5$, although the jet-center *Nu* peak at $y' = 0$ still remains less than the non-effusion level as compared in Fig. 9c and f, the improved heat transfer performances over the inter-jet regions

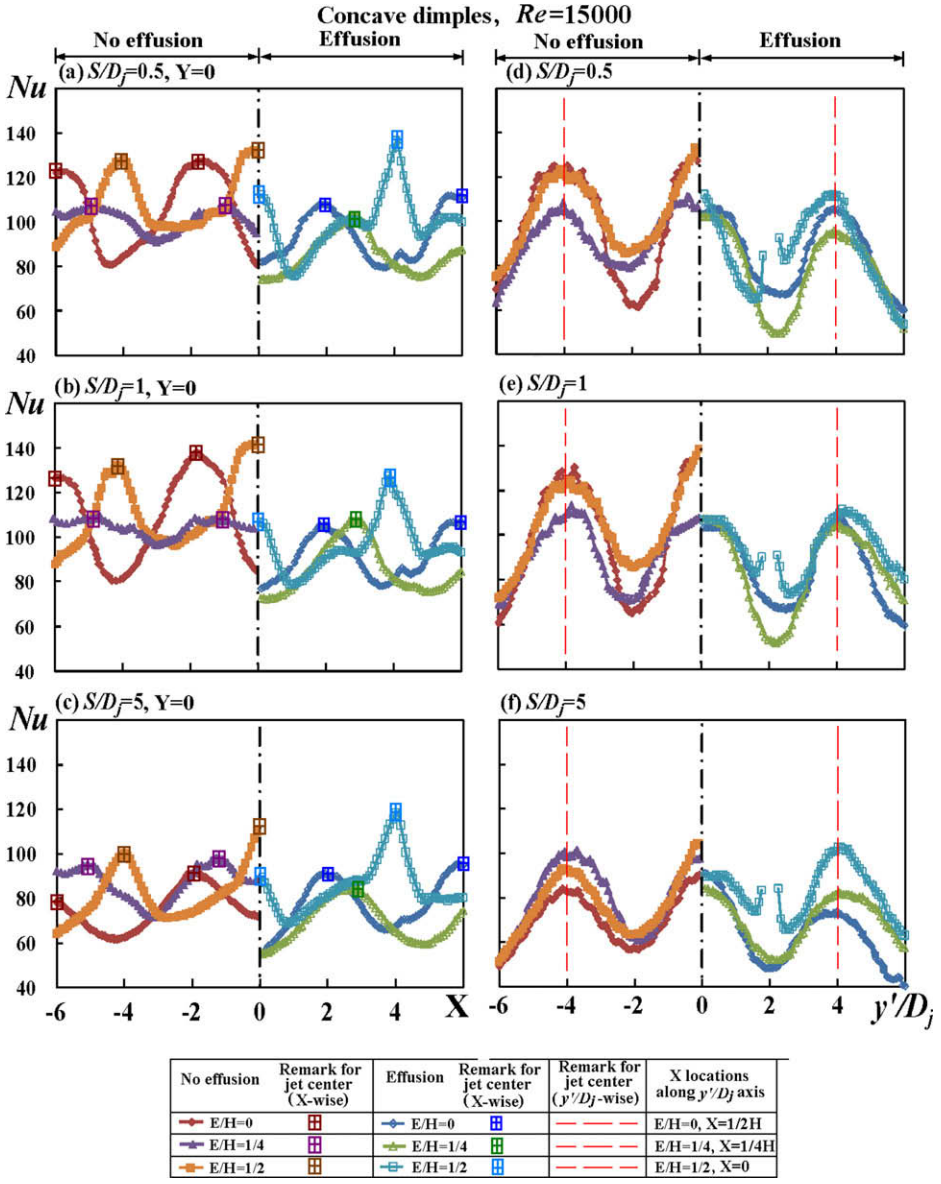

Fig. 9. *Nu* profiles along *X*-wise centerline and *y*′ axis over concave-dimpled surfaces with and without effusion at *Re* = 15,000 for S/D_j = 0.5, 1, 5.

on the effused surface from the non-effusion conditions can lead to $\overline{Nu}_C$ elevation from the non-effusion reference as previously demonstrated.

As described previously, one major consequence created by the different topologies between the concave and convex dimples is the larger wall-jet momentums required for the spent flows to upsurge the convex dimples in order to facilitate the HTE impacts produced by convex dimples. In the respect, the *Nu* ripples developed over the inter-jet regions on the non-effused surfaces with convex dimples along the *X*-wise *Nu* profiles at $E/H = 1/4$ and 1/2 as seen in Fig. 10a–c have been previously reported [29] as the major HTE impacts provided by these convex dimples. As the wall-jet momentum plays the more important role for HTE impacts produced by convex dimples, the heat transfer performances upon the impingements are closely affected by the *E*/*H* dependent surface topology that surrounds each stagnation point. In general, as *E*/*H* increases, the degrees of up-surging conditions for the wall-jet flows to traverse the convex dimples are enhanced. As a result, the jet-center *Nu* peaks at $y' = 0$ consistently follow the order of $Nu_{(E/H=0)} > Nu_{(E/H=1/4)} > Nu_{(E/H=1/2)}$ for all three S/D_j examined as shown in Fig. 10d–f. In addition to such dissimilar *E*/*H* impacts on the *Nu* peaks at $y' = 0$, the *E*/*H* impacts on the effusion-affected heat transfer performances over the inter-jet regions also vary with concave and convex dimples. As observed in Fig. 9, the different $\overline{Nu}_C$ for the effused surface with concave dimples between $E/H = 0$, 1/4 and 1/2 are mainly attributed to the *E*/*H*-driven *Nu* differences along *y*′ axis over the inter-jet regions as seen in Fig. 9d–f. But as compared in Fig. 10a–c for the effused surface with convex dimples, the oscillating amplitudes and stagnation *Nu* peaks in the *X*-wise *Nu* profiles with $E/H = 1/2$ are noticeably reduced from the effused counterparts with $E/H = 0$ and 1/4. The *E*/*H*-driven *Nu* differences along *X axis* over the inter-jet regions as seen in Fig. 10a–c have profound influences on the various $\overline{Nu}_C$ over the effused surface with convex dimples. Among three *E*/*H* tested with convex dimples and effusion, the *Nu* elevations over the inter-jet regions on the *X*-wise *Nu* profiles with $E/H = 1/2$ overweigh the reductions in stagnation *Nu* peaks from the counterparts with $E/H = 0$ and 1/

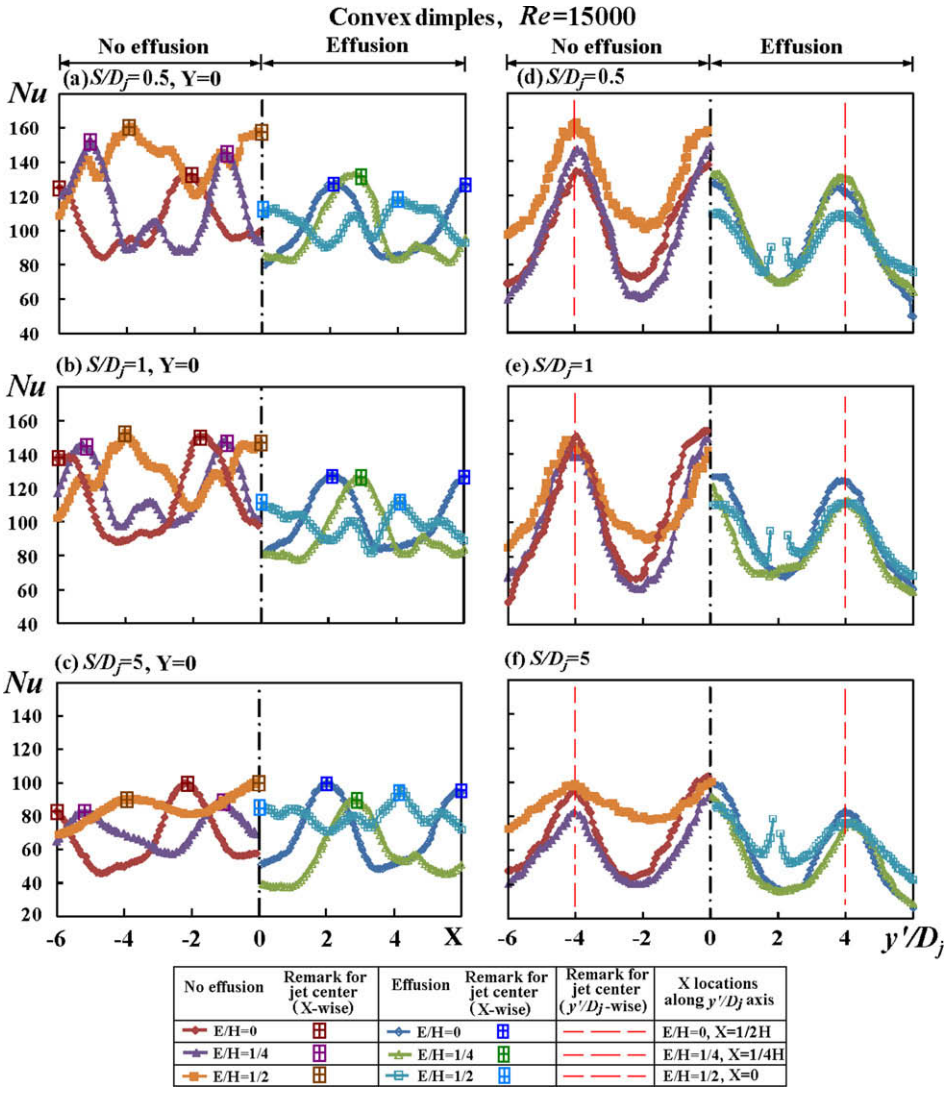

Fig. 10. *Nu* profiles along *X*-wise centerline and *y*′ axis over convex-dimpled surfaces with and without effusion at Re = 15,000 for S/D_j = 0.5, 1, 5.

4, which results in the higher $\overline{Nu}_C$ for $E/H = 1/2$. For the non-effusion results showed by Fig. 10, the highest $\overline{Nu}_C$ also develop at $E/H = 1/2$; while $\overline{Nu}_C$ at $E/H = 0$ and 1/4 fall in close agreements. But the extents of such E/H driven $\overline{Nu}_C$ differences between the effused and non-effused surfaces with convex dimples are larger than those developed between the likewise surfaces with concave dimples.

3.3. $\overline{Nu}_C$ performances and correlations

The complex Re, S/D_j and E/H effects on the detailed *Nu* distributions over the effused surfaces with concave and convex dimples are described in previous sections. As the aforementioned flow mechanisms are mutually affected, $\overline{Nu}_C$ over each effused surface roughened by dimples are interdependent with the controlling parameters of Re, S/D_j and E/H. Fig. 11 compares the varying manner of $\overline{Nu}_C$ versus Re for all the test results detected from the effused surfaces with concave and convex dimples. In each plot of Fig. 11, three $\overline{Nu}_C$ curves with $E/H = 0$, 1/4 and 1/2 at a fixed S/D_j are compared that reveals a general E/H-driven pattern of $\overline{Nu}_{C(E/H=1/2)} > \overline{Nu}_{C(E/H=0)} > \overline{Nu}_{C(E/H=1/4)}$. While the highest $\overline{Nu}_C$ still consistently emerge at $E/H = 1/2$ over each effused surface; $\overline{Nu}_C$ at $E/H = 0$ and 1/4 gradually fall into close agreements as S/D_j increases from 0.5 to 10. For each controlled impinging topology, $\overline{Nu}_C$ increases as Re increases but the slope of each data trend displayed in Fig. 11 varies with S/D_j and E/H. If the limiting condition of vanishing forced convection is designated as $\overline{Nu}_C = 0$ as $Re \to 0$, each data trends showed in Fig. 11 can be individually correlated by Eq. (1) for each effused surface with dimples.

$$\overline{Nu}_C = A\{S/D_j\} \times Re^{B\{S/D_j\}} \tag{1}$$

Coefficient A and exponent B in Eq. (1) are generated through the curve fitting routine based on the data collected in Fig. 11. The variations of coefficient A and exponent B against S/D_j for each E/H examined over the effused surface with concave or convex dimples are depicted in Fig. 12. As a general S/D_j-driven pattern disclosed in Fig. 12, coefficient A and exponent B are, respectively, decreased and increased by way of increasing S/D_j from 0.5 to 10. The varying trends of A and B are best fitted by the exponential functions which are indicated as the solid lines in each plot of Fig. 12. Six $\overline{Nu}_C$ correlations for two effused surfaces with concave or convex dimples at $E/H = 0$, 1/4 and 1/2

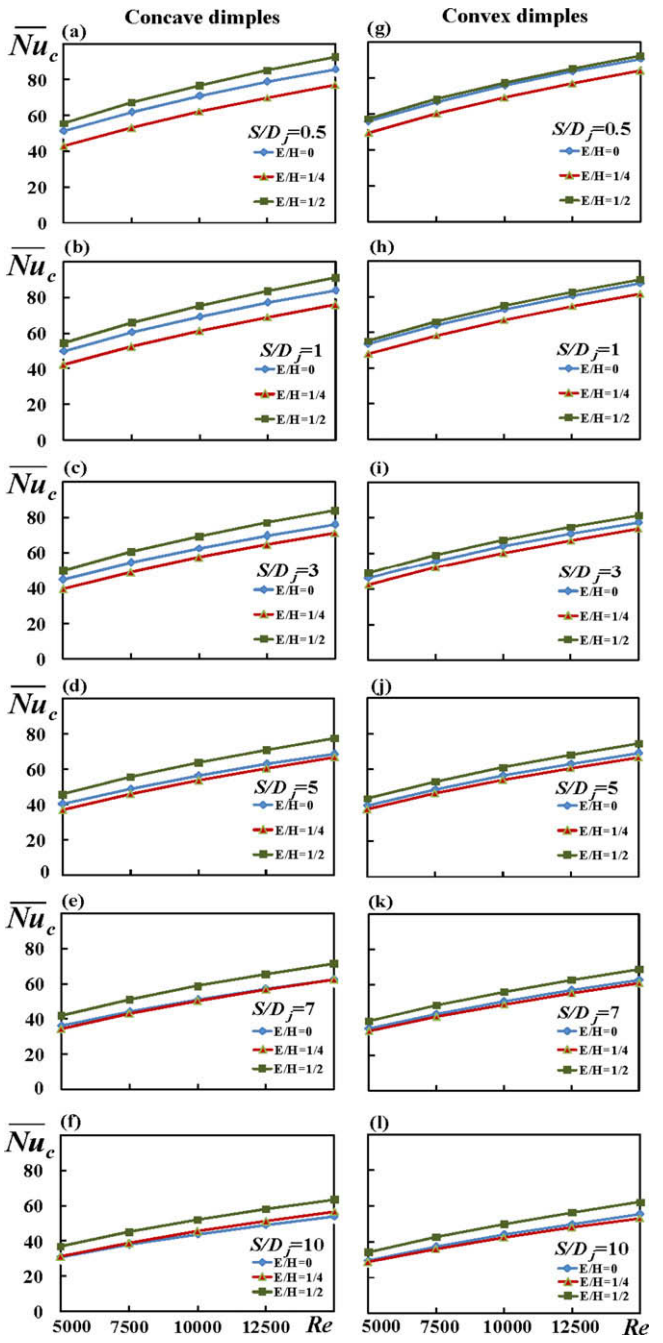

Fig. 11. Variations of $\overline{Nu}_C$ against Re for effused surfaces with concave and convex dimples at S/D_j = 0.5, 1, 3, 5, 7, 10.

are derived in Eqs. (2)–(7), respectively. The lowest correlation coefficients for A or B functions which are used to construct Eqs. (2)–(7) are 0.92, 0.95, 0.93, 0.95, 0.92 and 0.94, respectively.

$$\overline{Nu}_C = 1.012e^{-0.088\times S/Dj} \times Re^{0.465\times e^{0.0084\times S/Dj}}$$
(Concave dimples at $E/H = 0$) (2)

$$\overline{Nu}_C = 0.464e^{-0.0409\times S/Dj} \times Re^{0.534\times e^{0.0017\times S/Dj}}$$
(Concave dimples at $E/H = 1/4$) (3)

$$\overline{Nu}_C = 1.095e^{-0.069\times S/Dj} \times Re^{0.464\times e^{0.0063\times S/Dj}}$$
(Concave dimples at $E/H = 1/2$) (4)

$$\overline{Nu}_C = 1.409e^{-0.177\times S/Dj} \times Re^{0.437\times e^{0.0261\times S/Dj}}$$
(Convex dimples at $E/H = 0$) (5)

$$\overline{Nu}_C = 0.846e^{-0.127\times S/Dj} \times Re^{0.481\times e^{0.0157\times S/Dj}}$$
(Convex dimples at $E/H = 1/4$) (6)

$$\overline{Nu}_C = 1.501e^{-0.15\times S/Dj} \times Re^{0.431\times e^{0.0231\times S/Dj}}$$
(Convex dimples at $E/H = 1/2$) (7)

Eqs. (2)–(7) are specifically derived for the two sets of dimpled geometries with effusion. The performances of all the $\overline{Nu}_C$ correlations embodied in Eqs. (2)–(7) over the effused surfaces with concave and convex dimples are examined by comparing all the experimental measurements with the correlation predictions as indicated in Fig. 13. The maximum discrepancy of ±10% between the experimental and correlative results is achieved for 98% of the entire set of data generated. This set of experimentally based correlations offer the reasonable predictions for $\overline{Nu}_C$ using Re and S/D_j as the controlling parameters for each E/H examined here.

In addition to the Nu performance that reflects the convective capability for heat flux transferred, the additional heat transfer areas provided by the surface dimples need to be considered. The multiplication of $\overline{Nu}_C/\overline{Nu}_{C\ \text{Smooth wall}}$ and the area ratio between the dimpled and the smooth-walled surfaces ($A_C/A_{C\ \text{Smooth wall}}$) was previously quoted as 1.21 to highlight the relative enhancement of heat-transfer power over the impinging dimpled surface from the smooth-walled reference condition [30]. The index factor, namely $(\overline{Nu}_C/\overline{Nu}_{C\ \text{Smooth wall}}) \times (A_C/A_{C\ \text{Smooth wall}})$, is similarly adopted with the $\overline{Nu}_{C\ \text{Smooth wall}}$ referred to our previous works [29,30]. The variations of index factor against Re for three test conditions of E/H = 0, 1/4 and 1/2 at each S/D_j examined for the effused surfaces with concave or convex dimples are collected in each plot of Fig. 14. Also compared in Fig. 14 are the results detected from the likewise non-effused surfaces with dimples [29,30]. As well as the re-confirmation, the differences in the index factors between the effused and non-effused surfaces with either concave or convex dimples are systematically reduced as Re or/and S/D_j increase. At S/D_j = 10, 7, 5 as shown in Fig. 14f, e and d, the higher index factors for the effused surface with concave dimples at E/H = 1/2 over the non-effused counterparts initiate at Re = 10000, 12,500 and 15,000, respectively. But with convex dimples, the index factors detected from the effused surface remain consistently less than the non-effusion counterparts for the present test conditions. As a general trend as shown in Fig. 14, the index factors consistently increase as Re decreases or S/D_j increases for each dimpled surface with or without effusion. This general data trend indicates that the increase of S/D_j ratio can extend the effective Re range within which the index factors are above than unity. With $S/D_j > 3$, the index factors for each effused surface with concave or convex dimples are above than unity, suggesting the improving heat-transfer powers from the smooth-walled conditions. However, with $0.5 \leqslant S/D_j \leqslant 10$, all the index factors for concave and convex dimples collected in Fig. 14 for E/H = 1/2 are higher than unity. Thus the heat-transfer powers over each effused dimple-surface are increased from the non-effused smooth-wall references when E/H is controlled at 1/2.

4. Conclusions

This experimental study performed detailed Nu measurements over two effused impinging surfaces roughened by concave and convex dimples. Several salient points emerge from this study as summarized as follows:

1. Without effusion, the $\overline{Nu}_C$ with concave dimples are less than their counterparts with convex dimples. As the larger wall-jet momentums are required for the spent flows to upsurge the convex dimples in order to trip their HTE impacts, the larger

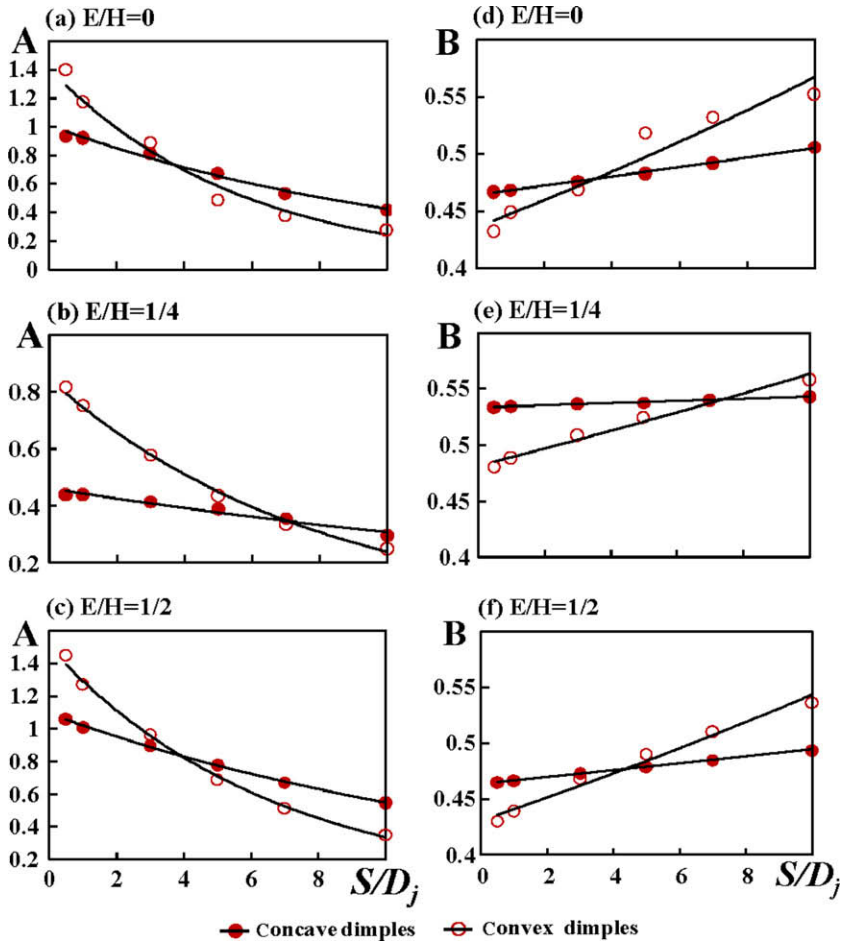

Fig. 12. Variations of coefficient A and exponent B in $\overline{Nu}_C$ for effused surfaces with concave and convex dimples.

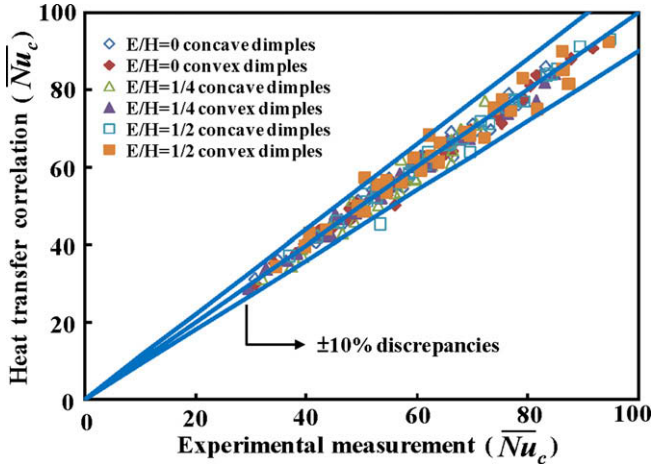

Fig. 13. Comparison of correlation results and experimental measurements for $\overline{Nu}_C$.

degrees of $\overline{Nu}_C$ differences between the effusion and non-effusion results consistently develop over the convex-dimpled surface. The Re and S/D_j above which the $\overline{Nu}_C$ over the effused surface with convex dimples exceed the non-effusion references are larger than those required by the concave dimpled surface.

2. Drastic Nu elevations around each effusion hole over each dimpled surface are observed. But the effective regions for such effusion-driven local HTE impacts are confined within one jet diameter over each dimpled surface.
3. Increase of S/D_j reduces the $\overline{Nu}_C$ differences between the effusion and non-effusion results for both concave- and convex-dimpled surfaces; while the HTE impacts generated by the impinging jet-array also fade out as S/D_j increases.
4. At each tested Re and S/D_j for both effused surfaces with concave or convex dimples, the general E/H-driven pattern of $\overline{Nu}_{C(E/H=1/2)} > \overline{Nu}_C(E/H=0) > \overline{Nu}_{C(E/H=1/4)}$ is observed. While the highest $\overline{Nu}_C$ still consistently emerge at $E/H = 1/2$ over both dimpled surfaces with effusions, $\overline{Nu}_C$ at $E/H = 0$ and 1/4 gradually fall into close agreements as S/D_j increases from 0.5 to 10.
5. For each dimpled surface at all E/H tested, the differences in $\overline{Nu}_C$ between non-effusion and effusion results consistently decrease as Re increases. The $\overline{Nu}_C$ over the concave-dimpled surface at each E/H examined recover at the faster rates than their convex counterparts as the higher momentums in wall-jet flows are required to stimulate the HTE impacts triggered by the protruding convex dimples.
6. A set of $\overline{Nu}_C$ correlations for two effused surfaces with concave and convex dimples is derived using Re and S/D_j as the controlling parameters at $E/H = 0$, 1/4 and 1/2.
7. The differences in the index factors between the effused and non-effused surfaces with concave or convex dimples are reduced as Re or/and S/D_j increase. Increase of S/D_j extends

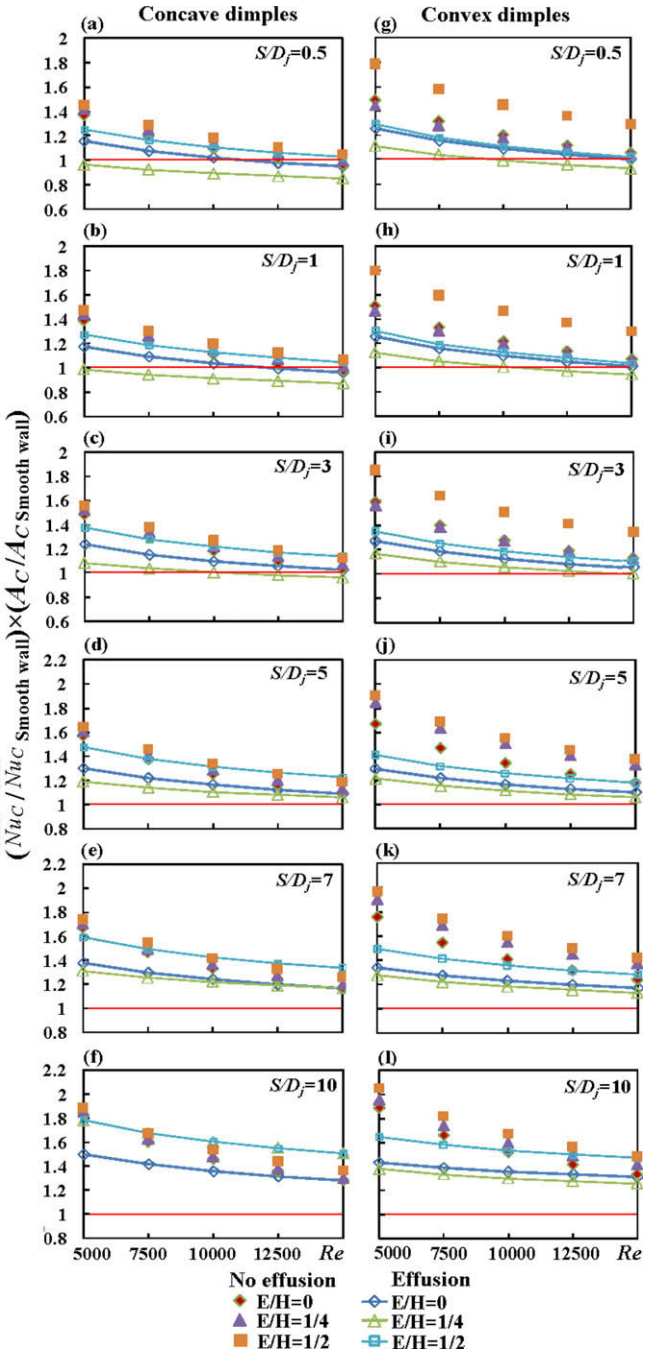

Fig. 14. Variations of index factor against *Re* for effused surfaces with concave and convex dimples at S/D_j = 0.5, 1, 3, 5, 7, 10.

the effective *Re* range within which the index factors are above than unity for both dimpled surfaces with effusions. Within the present *Re* and S/D_j ranges, all the index factors for each effused surface at $E/H = 1/2$ are higher than unity, which confirms the increases of heat-transfer power for each effused dimple-surface from the smooth-wall references at $E/H = 1/2$.

Acknowledgement

This research facility was financially supported by the National Science Council, R.O.C. under grant numbers NSC 96-2221-E-022-015MY3 and NSC 97-2221-E-022-013-MY3.

References

[1] R.J. Goldstein, W.S. Seoul, Heat transfer to a row of impinging circular air jets including the effect of entrainment, Int. J. Heat Mass Transfer 34 (1991) 2133–2147.
[2] D.E. Metzger, R.J. Korstad, Effects of crossflow on impingement heat transfer, ASME J. Eng. Power 94 (1972) 35–42.
[3] L.W. Florschuetz, R.A. Berry, D.E. Metzger, Periodic streamwise variation of heat transfer coefficients for inline and staggered arrays of circular jets with crossflow of spent air, ASME J. Heat Transfer 102 (1) (1980) 132–137.
[4] L.W. Florschuetz, C.R. Truman, D.E. Metzger, Streamwise flow and heat transfer distribution for jet impingement with crossflow, ASME J. Heat Transfer 103 (2) (1981) 337–342.
[5] L.W. Florschuetz, D.E. Metzger, C.C. Su, Y. Isoda, H.H. Tseng, Heat transfer characteristics for jet array impingement with initial crossflow, ASME J. Heat Transfer 106 (1) (1984) 34–41.
[6] N. Obot, T.A. Trabold, Impingement heat transfer within arrays of circular jets. Part I. Effects of minimum, intermediate, and complete crossflow for small and large spacings, ASME J. Heat Transfer 109 (4) (1987) 872–879.
[7] A.M. Huber, R. Viskanta, Convective heat transfer to a confined impinging array of air jets with spent air exits, ASME J. Heat Transfer 116 (1994) 570–576.
[8] Y. Huang, S.V. Ekkad, J.C. Han, Detailed heat transfer distributions under an array of orthogonal impinging jets, J. Thermophys. Heat Transfer 12 (1) (1998) 73–79.
[9] D.K. Lee, K. Vafai, Comparative analysis of jet impingement and microchannel cooling for high heat flux application, Int. J. Heat Mass Transfer 42 (1999) 1555–1568.
[10] B.P.E. Dano, J.A. Liburdy, K. Kanokjaruvijit, Flow characteristics and heat transfer performances of a semi-confined impinging array of jests: effect of nozzle geometry, Int. J. Heat Mass Transfer 48 (2005) 691–701.
[11] L. Huang, M.S. El-Genk, Heat transfer and flow visualization experiments of swirling, multi-channel, and conventional impinging jets, Int. J. Heat Mass Transfer 41 (1998) 583–600.
[12] L.M. Su, S.W. Chang, Detailed hest transfer measurements of impinging jet arrays issued from grooved surface, Int. J. Therm. Sci. 41 (2002) 823–841.
[13] A.I. Behbahani, R.J. Goldstein, Local heat transfer to staggered arrays of impinging circular air jets, ASME J. Eng. Power 105 (1983) 354–360.
[14] Y. Pan, B.W. Webb, Heat transfer characteristics of arrays of free-surface liquid jets, ASME J. Heat Transfer 117 (1995) 878–883.
[15] A.M. Huber, R. Viskanta, Effect of jet-to-jet spacing on convective heat transfer to confined, Impinging arrays of axisymmetric air jets, Int. J. Heat Mass Transfer 37 (1994) 2859–2869.
[16] R. Viskanta, Heat transfer to impinging isothermal gas and flame jets, Exp. Therm. Fluid Sci. 6 (1993) 111–134.
[17] S.C. Arjocu, J.A. Liburdy, Identification of dominant heat transfer modes associated with the impingement of an elliptical jet array, ASME J. Heat Transfer 122 (2000) 240–247.
[18] E.M. Sparrow, B.J. Lovell, Heat transfer characteristics of an obliquely impinging circular jet, ASME J. Heat Transfer 102 (1980) 202–209.
[19] A.J. Robinson, E. Schnitzler, An experimental investigation of free and submerged miniature liquid jet array impingement heat transfer, Exp. Therm. Fluid Sci. 32 (2007) 1–13.
[20] C. Gau, C.M. Chung, Surface curvature effect on slot-air-jet impingement cooling flow and heat transfer process, ASME J. Heat Transfer 113 (1991) 858–864.
[21] C. Gau, C.C. Lee, Impingement cooling flow structure and heat transfer along rib-roughened walls, Int. J. Heat Mass Transfer 35 (1992) 3009–3020.
[22] S. Parneix, M. Behnia, P.A. Durbin, Prediction of turbulent heat transfer in an axisymmetric jet impinging on a heated pedestal, ASME J. Heat Transfer 121 (1999) 43–49.
[23] Y. Kondo, H. Matsushima, T. Komatsu, Optimization of pin-fin Heat sink for impingement cooling in electronic packaging, ASME J. Electron. Packag. 122 (2000) 240–246.
[24] C. Gau, I.C. Lee, Flow and impinging cooling heat transfer along triangular rib-roughened walls, Int. J. Heat Mass Transfer 43 (2000) 4405–4418.
[25] E.E.M. Olsson, L.M. Ahrne, A.C. Trägårdh, Heat transfer from a slot air jet impinging on a circular cylinder, J. Food Eng. 63 (2004) 393–401.
[26] S.W. Chang, L.M. Su, Y. Zheng, Reciprocating impingement jet heat transfer with surface rib, J. Exp. Heat Transfer 13 (2000) 275–297.
[27] S.V. Ekkad, D. Kontrovitz, Jet impingement heat transfer on dimpled target surfaces, Int. J. Heat Fluid Flow 23 (2002) 22–28.
[28] K. Kanokjaruvijit, R.F. Martinez-botas, Jet impingement of a dimpled surface with different crossflow schemes, Int. J. Heat Mass Transfer 48 (2005) 161–170.
[29] S.W. Chang, Y.J. Jan, S.F. Chang, Heat transfer of impinging jet array over convex dimpled surface, Int. J. Heat Mass Transfer 49 (2006) 3045–3059.
[30] S.W. Chang, S.F. Chiou, S.F. Chang, Heat transfer of impinging jet array over concave dimpled surface with applications to cooling of electronic chipsets, Exp. Therm. Fluids Sci. 31 (2007) 625–640.
[31] B.R. Hollworth, L. Dagan, Arrays of impinging jets with spent fluid removal through vent holes on the target surface. Part I. Average heat transfer, ASME J. Eng. Power 102 (1980) 994–999.

[32] K. Garrett, B.W. Webb, The effect of drainage configuration on heat transfer under an impinging liquid jet array, ASME J. Heat Transfer 121 (1999) 803–810.
[33] D.-H. Rhee, P.-H. Yoon, H.H. Cho, Local heat/mass transfer and flow characteristics of array impinging jets with effusion holds ejecting spent air, Int. J. Heat Mass Transfer 46 (2003) 1049–1061.
[34] L.B.Y. Aldabbagh, I. Sezai, Three-dimensional numerical simulation of an array of impinging laminar square jets with spent fluid removal, Int. J. Therm. Sci. 43 (2004) 241–247.
[35] Editorial Board of ASME Journal of Heat Transfer, Journal of heat transfer policy on reporting uncertainties in experimental measurements and results, ASME J. Heat Transfer 115 (1993) 5–6.